Report

Current Biology

A Biosensor for the Mitotic Kinase MPS1 Reveals Spatiotemporal Activity Dynamics and Regulation

Highlights

- Development of a FRET-based biosensor of MPS1 kinase activity
- Active MPS1 detected at centromeres and chromatin is derived from kinetochores
- MPS1 activity is initiated ~12 min before NEB in a PP2A-B56-dependent manner
- Colon cancer cell lines and organoids have lower MPS1 activity than healthy lines

Authors

Timo E.F. Kuijt, Maaike L.A. Lambers, Sonja Weterings, Bas Ponsioen, Ana C.F. Bolhaqueiro, Debbie H.M. Staijen, Geert J.P.L. Kops

Correspondence

g.kops@hubrecht.eu

In Brief

Kuijt et al. use a FRET-based biosensor to examine the activity dynamics of the mitotic kinase MPS1. MPS1 activation is initiated at kinetochores before NEB and regulated by PP2A-B56. The extent of MPS1 activity in prometaphase is modulated by kinetochore-microtubule attachments and is diminished in colorectal cancer cells and organoids.

Kuijt et al., 2020, Current Biology *30*, 3862–3870
October 5, 2020
https://doi.org/10.1016/j.cub.2020.07.062

CellPress

CellPress
OPEN ACCESS

Current Biology

Report

A Biosensor for the Mitotic Kinase MPS1 Reveals Spatiotemporal Activity Dynamics and Regulation

Timo E.F. Kuijt,[1] Maaike L.A. Lambers,[1] Sonja Weterings,[1] Bas Ponsioen,[2,3] Ana C.F. Bolhaqueiro,[1] Debbie H.M. Staijen,[1] and Geert J.P.L. Kops[1,4,*]

[1]Oncode Institute, Hubrecht Institute-KNAW and University Medical Centre Utrecht, 3584CT Utrecht, the Netherlands
[2]Cancer Genomics Netherlands, UMC Utrecht, 3584CG Utrecht, the Netherlands
[3]Molecular Cancer Research, Centre for Molecular Medicine, UMC Utrecht, 3584CG Utrecht, the Netherlands
[4]Lead Contact
*Correspondence: g.kops@hubrecht.eu
https://doi.org/10.1016/j.cub.2020.07.062

SUMMARY

Accurate chromosome segregation during cell division critically depends on error correction of chromosome-spindle interactions and the spindle assembly checkpoint (SAC) [1–3]. The kinase MPS1 is an essential regulator of both processes, ensuring full chromosome biorientation before anaphase onset [3, 4]. To understand when and where MPS1 activation occurs and how MPS1 signaling is modulated during mitosis, we developed MPS1sen, a sensitive and specific FRET-based biosensor for MPS1 activity. By placing MPS1sen at different subcellular locations, we show that MPS1 activity initiates in the nucleus ~9–12 min prior to nuclear envelope breakdown (NEB) in a kinetochore-dependent manner and reaches the cytoplasm at the start of NEB. Soon after initiation, MPS1 activity increases with switch-like kinetics, peaking at completion of NEB. We further show that timing and extent of pre-NEB MPS1 activity is regulated by Aurora B and PP2A-B56. MPS1sen phosphorylation declines in prometaphase as a result of formation of kinetochore-microtubule attachments, reaching low but still detectable levels at metaphase. Finally, leveraging the sensitivity and dynamic range of MPS1sen, we show deregulated MPS1 signaling dynamics in colorectal cancer cell lines and tumor organoids with diverse genomic instability phenotypes.

RESULTS AND DISCUSSION

Accurate chromosome segregation requires biorientation of all chromosomes before the onset of anaphase. Central to guarding chromosome segregation fidelity is the mitotic kinase MPS1 [4]. Its activation causes phosphorylation of various substrates that promote efficient correction of erroneous kinetochore-microtubule attachments and a robust response of the SAC to lack of such attachments [1, 2]. Conversely, inhibition of MPS1 upon biorientation is necessary for timely cell-cycle progression [5, 6]. Much can be learned concerning maintenance of chromosomal stability from studying mechanisms and dynamics of MPS1 activation prior to and during mitosis and of its subsequent inactivation. FRET-based biosensors have uncovered localized regulation of mitotic kinase activity and greatly increased our understanding of their signaling pathways in single cells [7–9]. Inspired by these studies, we set out to develop a FRET-based biosensor specific for MPS1 kinase in order to study its (de)activation dynamics during mitosis.

MPS1sen Is a Specific Biosensor for MPS1 Kinase

To study spatiotemporal dynamics of MPS1 kinase signaling, we modified an existing PLK1 biosensor with the substrate sequence LLLDS(pThr)LSINW, previously shown to be also targeted by MPS1 during mitosis [10, 11]. Substrate consensus motifs for MPS1 and PLK1 kinases are similar in some positions (e.g., negative charges at −2 or −3 relative to phosphorylated S/T) but also have distinct features [12, 13]. We utilized these distinctions to increase specificity of the sensor for MPS1 kinase. We introduced a glycine at position −1, an additional negative charge at −3, and an alanine at +2, creating the substrate sequence LLEDG(pThr)LIANW. We furthermore optimized the dynamic range of the sensor by inserting higher quantum yield fluorophores (Figure 1A).

A prominent pool of active MPS1 is located at the outer kinetochore where it binds to the HEC1/NUF2 components of the NDC80 complex [14–16]. To verify specificity of the biosensor (hereafter named MPS1sen), we placed it close to the MPS1 activation site by fusion to the N terminus of SPC24 (hereafter named MPS1sen-KT). We then monitored FRET (mTurquoise2/YPet ratio after mTurquoise excitation) in mitotic HeLa cells treated with the spindle poison nocodazole. MPS1sen-KT showed a robust FRET signal, which was abolished upon inhibition of MPS1 by the small-molecule inhibitor Cpd-5 [17] (Figures 1B and 1C) or upon depletion of MPS1 by RNAi (Figures S1A and S1B). Importantly, despite similarity in consensus substrate sequences and overlapping localization [12, 13, 18], inhibition of PLK1 with BI-2536 [19] did not reduce FRET, further validating specificity of MPS1sen (Figures 1B and 1C). Aurora B prefers basic amino acids at position −2 and −3 instead of acidic ones [12], and indeed the Aurora B inhibitor ZM447439 [20] did not prevent MPS1sen phosphorylation. In line with the known

CellPress
OPEN ACCESS

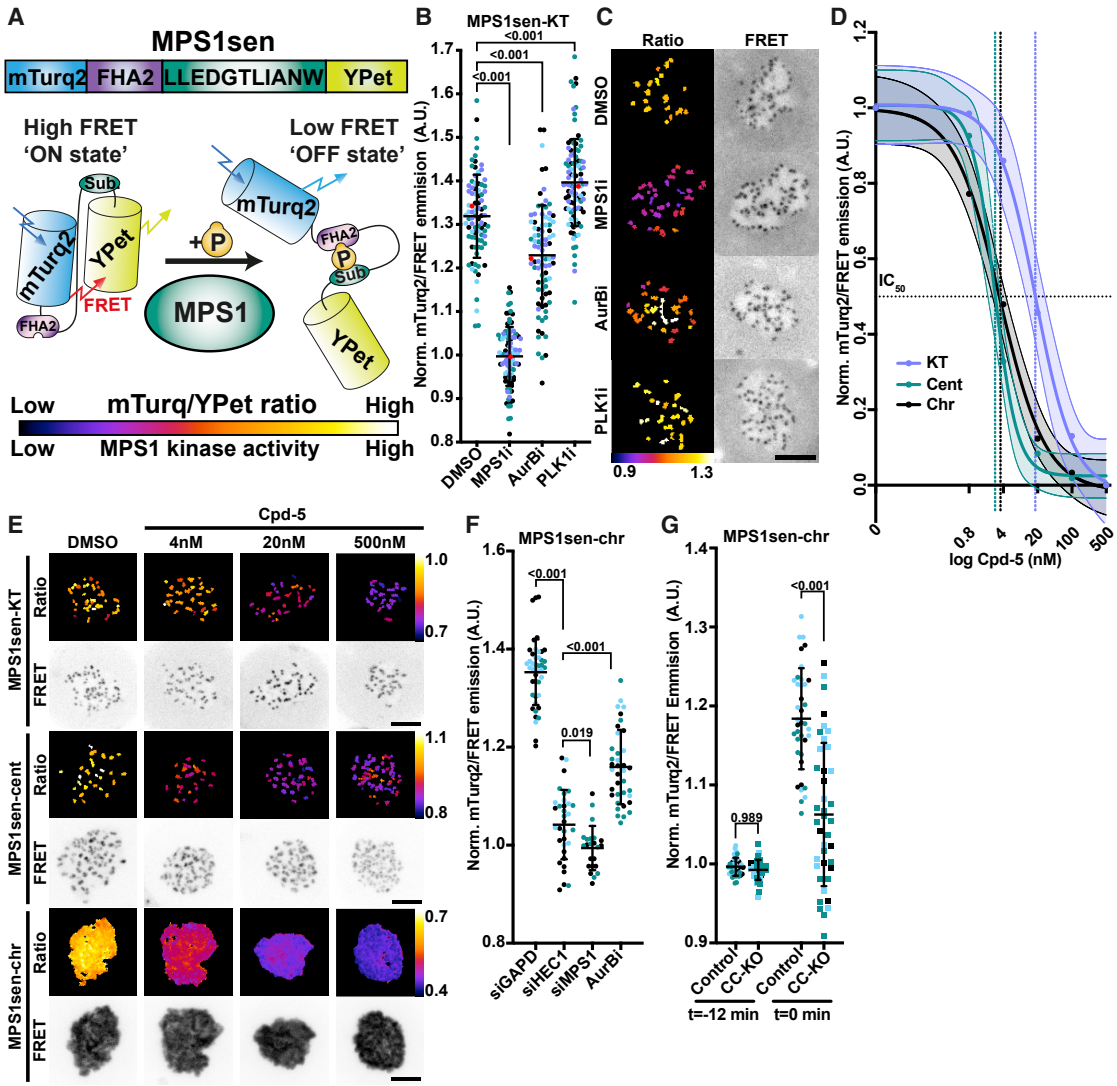

Figure 1. Cellular MPS1 Kinase Activity, Measured by the Specific Sensor MPS1sen, Originates from Kinetochores

(A) Cartoon of MPS1sen design. MPS1sen FRET efficiency decreases by virtue of phosphorylation of the substrate sequence. The pseudo-colored calibration bar represents low (dark purple) to high (yellow/white) MPS1 activity.

(B and C) HeLa cells stably expressing MPS1sen-KT, arrested in prometaphase (nocodazole) for 1 h and treated with indicated inhibitors for 45 min (+MG-132).

(B) Quantification of MPS1sen-KT FRET (local ratio), normalized to MPS1i (500 nM Cpd-5) condition (mean ± SD). Each data point represents mean FRET ratio of multiple kinetochores per cell. Data point colors indicate individual repeats of experiment (N = 4), and the red symbol indicates the data point used as representative image (C).

(C) Representative images of data shown in (B) where the maximum projected FRET (YFP) channel and object ratio (pseudo-colored, real ratio values indicated) images are scaled identically for direct comparison. Scale bar, 5 μm.

(D) Quantification of FRET ratios (MPS1sen-KT [N = 4], MPS1sen-cent [N = 2], or MPS1sen-chr [N = 3]) in cells arrested in mitosis with nocodazole and subsequently treated with MG-132 and Cpd-5 for 45–60 min before imaging. Mean FRET ratio (±95% CI) of MPS1sen per location was normalized and plotted on y axis, and MPS1i concentrations were converted to log scale (x axis) followed by nonlinear least square regression ($R^2 \geq 0.94$).

(E) Images from cells quantified in (D), scaled to compare per biosensor location and real ratio values indicated, scale bar, 5 μm.

(F) Quantification of FRET ratios from HeLa cells expressing MPS1sen-chr treated with indicated siRNAs for 48 h or a small-molecule inhibitor. Data were extracted from Figure S3A (siGAPD, siHEC1, siMPS1) or Figure 3G (siGAPD + AurBi) at time point 30 min post-NEB (mean ± SD is shown).

(G) Quantification of inducible Cas9 HeLa CENP-C knockout (CC-KO, square symbols) cells and control (round symbols) expressing MPS1sen-chr. Live cell imaging was performed after 96 h doxycycline induction and data from 12 min. before NEB and moment of NEB are shown (mean ± SD, N ≥ 3).

See also Figure S1.

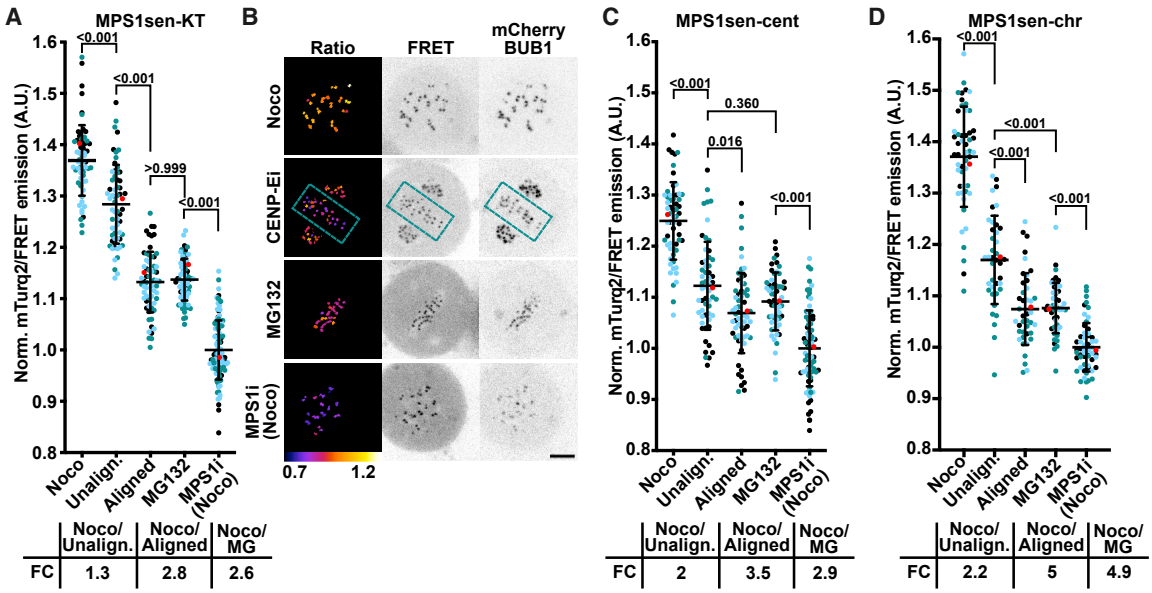

Figure 2. Kinetochore-Microtubule Interactions Regulate MPS1 Activity throughout the Cell

(A, C, and D) Quantification of FRET ratios from HeLa cells expressing MPS1sen at various locations and arrested in mitosis using indicated compounds for 45 min. In CENP-E-inhibited cells, FRET ratios on aligned versus unaligned chromosomes were calculated. Ratios were normalized to Noco+MPS1i condition. Each data point represents multiple kinetochores/centromeres/chromosomes per cell (mean ± SD). Colors of data points represent data from independent repeats of experiment (N = 3), and the red symbol indicates the data point used as representative images in (B).

(B) Representative images of data quantified in (A). Box (teal color) in CENP-Ei condition indicates the kinetochores quantified as "aligned." Images are equally scaled for comparison per biosensor location and real ratio values are indicated, scale bar, 5 μm.

See also Figure S2.

role of Aurora B in promoting MPS1 activity during mitosis [21–23], we observed a slight but significant reduction of FRET, illustrating the ability of MPS1sen to report on minor changes to MPS1 activity states. MPS1sen-KT showed similar dynamic range and responded similarly to inhibition of Aurora B or PLK1 in non-transformed RPE-1 cells (Figures S1C and S1D). Taken together, we conclude that MPS1sen is a specific reporter for MPS1 with a dynamic range that enables it to detect relatively subtle changes to MPS1 activity.

MPS1 Activity Originates at Kinetochores

To examine whether MPS1 activity can be detected beyond the kinetochore, we placed MPS1sen at centromeres or chromatin by fusing it to CENP-B (MPS1sen-cent) or histone H2B (MPS1sen-chr), respectively. In agreement with reported MPS1 substrates at these locations [24, 25], both MPS1sen-cent and MPS1sen-chr revealed substantial MPS1 activity, which was sensitive to cpd-5 (Figures 1D and 1E). The MPS1 activity reported by these probes originated from kinetochores, as evidenced by the following observations: first, FRET signals in mitotic cells were strongly reduced following HEC1 depletion by RNAi or Aurora B inhibition by ZM447439 (Figures 1F, S1E, and S1F). Second, conditional knockout of CENP-C [26] in roughly half the cell population (Figure S1G) abolished or strongly reduced FRET signals in a similar fraction of cells (Figures 1G, S1H, and S1I). Assembly of the outer kinetochore is thus required for generating most if not all cellular MPS1 activity. Third, if MPS1 reaches distant sites by spreading from kinetochores, we reasoned that this should result in local differences in the concentration of active molecules. In support of this, full inhibition of MPS1 at kinetochores required 500 nM of Cpd-5 (IC_{50} 18 nM) while at more kinetochore-distal locations 100 nM Cpd-5 sufficed (IC_{50} 2–3 nM) (Figures 1D and 1E). Although differences in phosphatase activities at these various sites may exist, our data are consistent with a model in which MPS1 is activated at the outer kinetochore by binding the NDC80 complex and subsequently travels to distant sites. In prophase, for example, if sufficient MPS1 can be activated at kinetochores (see below), this would then allow phosphorylation of condensin II [25] and nuclear pore- MAD1 complexes [27–29].

Kinetochore-Microtubule Interactions Regulate MPS1 throughout the Cell

We and others have shown that formation of end-on kinetochore-microtubule attachments disrupt the MPS1-HEC1/NUF2 interaction and can silence the SAC in the absence of tension [15, 16, 30–32]. Our MPS1 biosensor allowed us to examine how MPS1 substrate phosphorylation is affected by various kinetochore-microtubule attachment configurations. To this end, we modulated kinetochore-microtubule attachments using various perturbations in cells expressing MPS1sen-KT. In these cells, mCherry-BUB1 [33] was expressed from the endogenous locus to monitor whether and how BUB1 kinetochore localization correlates with MPS1 activity. While unattached kinetochores in nocodazole-treated cells displayed high MPS1sen-KT phosphorylation, stably bioriented kinetochores at metaphase in MG132-treated cells showed low phosphorylation that was further reduced by addition of Cpd-5 (Figures 2A, 2B, and

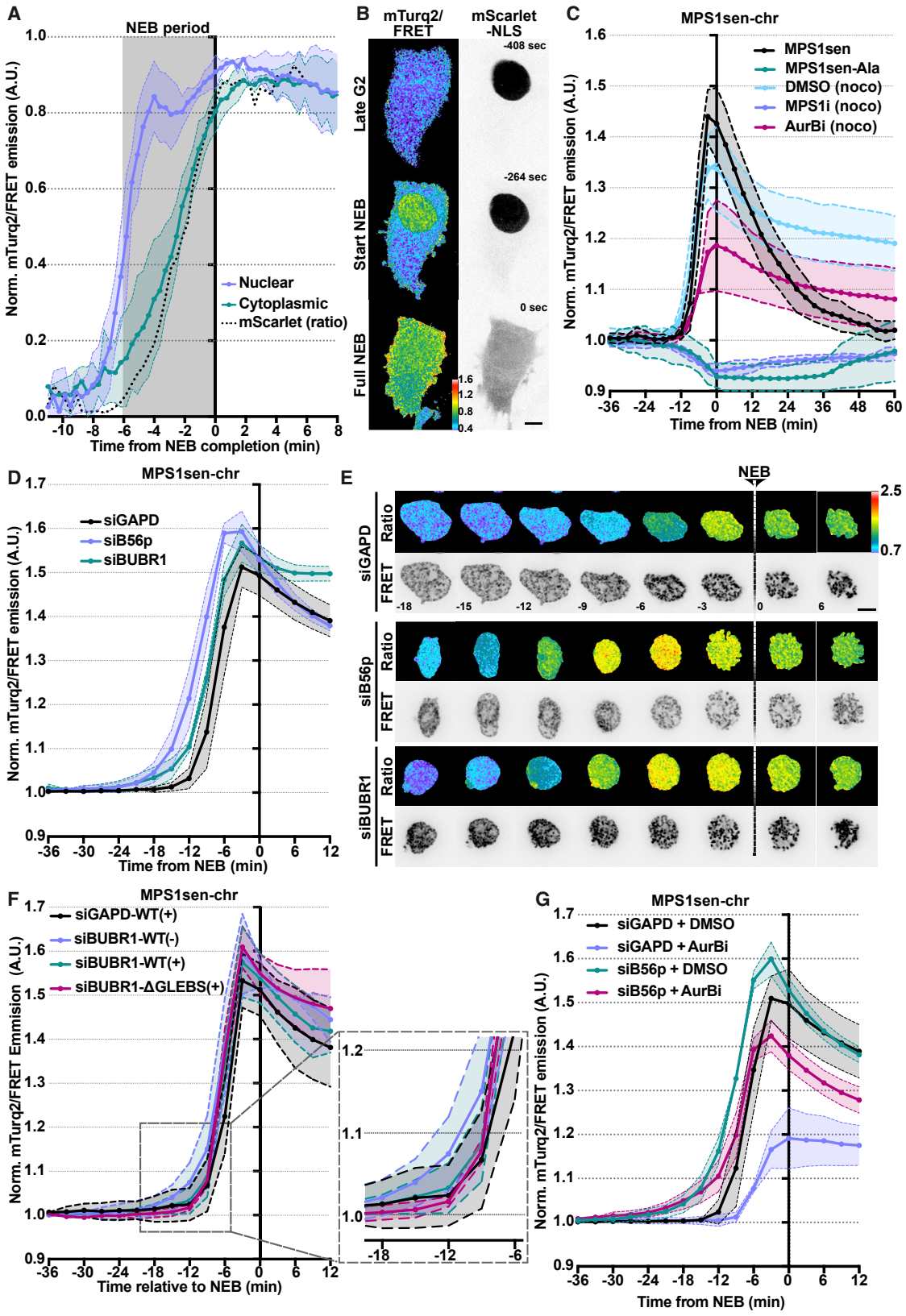

(legend on next page)

S2A). MPS1 thus displays detectable activity in metaphase. This is in line with residual levels of BUB1 (Figures 2B and S2F; [33]) and KNL1 phosphorylation [15, 33, 34] on metaphase kinetochores, and with observations that targeting of MAD1 to metaphase kinetochores re-elicits an MPS1-dependent SAC response [35–37]. The reason for residual MPS1 activity in metaphase is unclear. Since we observed occasional loss of metaphase plate integrity upon MPS1 inhibition (Figures S2B and S2D), perhaps it functions to maintain correct microtubule dynamics or retain some BUB1-SGO1 (Figure S2F) to promote centromeric CPC localization and thus preserve sister chromatid cohesion [38, 39]. Low metaphase MPS1 activity could additionally aid in fast SAC reactivation upon loss of kinetochore-microtubule attachments.

To directly compare various attachment states in a single cell, we inhibited the kinesin CENP-E. Cells with inactive CENP-E have many bioriented chromosomes at the metaphase plate and a few unaligned (unattached or transiently attached) ones near centrosomes [40, 41]. MPS1sen-KT phosphorylation on kinetochores of those bioriented chromosomes was as low as on those of metaphase cells (Figures 2A, 2B, S2A, and S2B). On kinetochores of unaligned chromosomes, however, MSP1sen-KT was highly phosphorylated. Similar results were obtained in RPE-1 cells (Figure S2G). Interestingly, BUB1 levels at kinetochores did not fully correlate with MPS1sen-KT phosphorylation under these conditions (Figure S2F), suggesting there may be MPS1-independent regulation of BUB1 at kinetochores [34, 42]. MPS1sen modulations by attachment states were generally recapitulated by placing it on centromeres or chromatin. Interestingly, however, on unaligned chromosomes in CENP-E-inhibited cells, MPS1sen phosphorylation on centromeres was substantially lower than on kinetochores (Figures 2C, 2D, and S2C–S2H). The reason for this is unclear. Perhaps it reflects differences in local phosphatase activities or in the ability of MPS1 to reach centromeric chromatin regions in these cells. Taken together, the data show that kinetochore-microtubule interactions and chromosome biorientation modulate MPS1 kinase signaling throughout the cell.

Switch-like Activation of MPS1 in the Prophase Nucleus

Kinase biosensors revealed that nuclear translocation of cyclin B/CDK1 in prophase does not restrict CDK1 activity solely to the nucleus [43] and that PLK1 activity is restricted to the nucleus in G2 phase [10]. MPS1 localizes to the cytoplasm in interphase and translocates to the nucleus upon mitotic entry [44, 45]. To visualize the spatial dynamics of MPS1 activation, we expressed MPS1sen without specifying its subcellular localization, resulting in nuclear and cytoplasmic pools. We co-expressed mScarlet-NLS to accurately monitor nuclear envelope breakdown (NEB). Phosphorylation of nuclear MPS1sen became apparent roughly 10 min before completion of NEB, while phosphorylation of cytoplasmic MPS1sen was delayed by several minutes (Figures 3A and 3B; Video S1). Phosphorylation of this pool correlated with leakage of mScarlet-NLS (cytoplasmic/nuclear ratio) from the nucleus as NEB commenced. These data agree with a recent observation that MPS1 kinetochore localization correlates with nuclear import of cyclin B [45] and suggest MPS1 is activated in the nucleus.

To more accurately monitor pre-mitotic activation of MPS1, we next wished to immobilize MPS1sen in the nucleus. Unfortunately, MPS1sen-KT was hardly detectable at early prophase kinetochores, likely due to immature outer-kinetochore assembly [46]. We thus opted to use MPS1sen-chr, as it is stably bound to chromatin throughout the cell cycle and correctly reports on kinetochore-derived MPS1 activity (see Figures 1D–1F and also an additional mutation of the substrate sequence in Figure 3C). In further support of this, MPS1sen-chr did not show any phosphorylation during mitotic progression of MPS1-inhibited or -depleted cells (Figures 3C and S3A). This was not an indirect effect of SAC inactivation, because MAD2 depletion hardly impacted MPS1sen-chr phosphorylation (Figure S3A). Notably, during a normal, unperturbed mitosis, MPS1sen-chr phosphorylation was detectable 9–12 min before full NEB (monitored by mScarlet-NLS [Video S2]), rapidly increased thereafter, and peaked around completion of NEB (Figure 3C). This switch-like activation was more rapid than that of PLK1 [10] and resembled the activation kinetics of cyclin B1/CDK1 [43]. As cells progressed from prometaphase to metaphase, MPS1sen-chr phosphorylation decreased and the FRET ratio returned to pre-mitotic levels as cells exited mitosis (45–60 min after NEB) (Figure 3C).

Timing of Prophase MPS1 Activation Is Regulated by PP2A-B56

Our data showed that MPS1sen-chr phosphorylation starts in prophase and is maximal by the time of completion of NEB (Figures 3A–3C), consistent with a prominent role for CDK1 in MPS1 activation [16, 21, 47, 48]. We next wished to investigate which other activities regulate dynamics of prophase MPS1 activation. To obtain more insights into a previously reported role for Aurora B

Figure 3. Prophase MPS1 Activation Dynamics Are Regulated by PP2A-B56 and Aurora B

(A) Quantification of FRET ratios (mean ± SD, N ≥ 3) of HeLa cells expressing MPS1sen, released from overnight G2-block (RO-3306). Cells entered mitosis in 6.6 μM Noco while imaging (every ± 24 s). The black dotted line represents mScarlet-NLS ratio (Cytoplasm/Nuclear) to define start and completion of NEB (marked in gray).

(B) Images of data quantified in (A), extracted from Video S1. Images are scaled equally for comparison, scale bar , 10 μm.

(C) Quantification of FRET ratio (mean ± SD, N ≥ 3) of HeLa cells expressing H2B-MPS1sen-chr or H2B-MPS1sen-Ala-chr (non-phosphorylatable mutant), progressing through mitosis (in 2 replicates with mScarlet-NLS, see Video S2). Cells entered mitosis in Noco and proTAME (to delay exit of MPS1i cells) and were treated with indicated compounds before mitotic entry. Data are normalization at t = −51 min relative to NEB on the population average of each condition.

(D) Quantification of FRET ratio (mean ± SD, N ≥ 3) of HeLa cells expressing H2B-MPS1sen-chr and transfected with siRNAs to the indicated proteins for 14 h, followed by 24 h thymidine block. Cells were released for 6 h after which Noco was added before start of imaging. Data were processed as described for (C).

(E) Representative images of data quantified in (D) t = 0 is frame after full NEB, scaled equally, scale bar, 10 μm.

(F) Similar to (D), however, only cells that expressed BUBR1-WT (in siGAPD or siBUBR1) or BUBR1-ΔGLEBS were quantified. An enlargement of the moment preceding NEB is placed to highlight the rescue of premature MPS1 activation by BUBR1-ΔGLEBS expression.

(G) Similar to (D), with the difference that cells were imaged in presence of 2 μM ZM447439 (AurBi) or solvent (DMSO).

See also Figure S3.

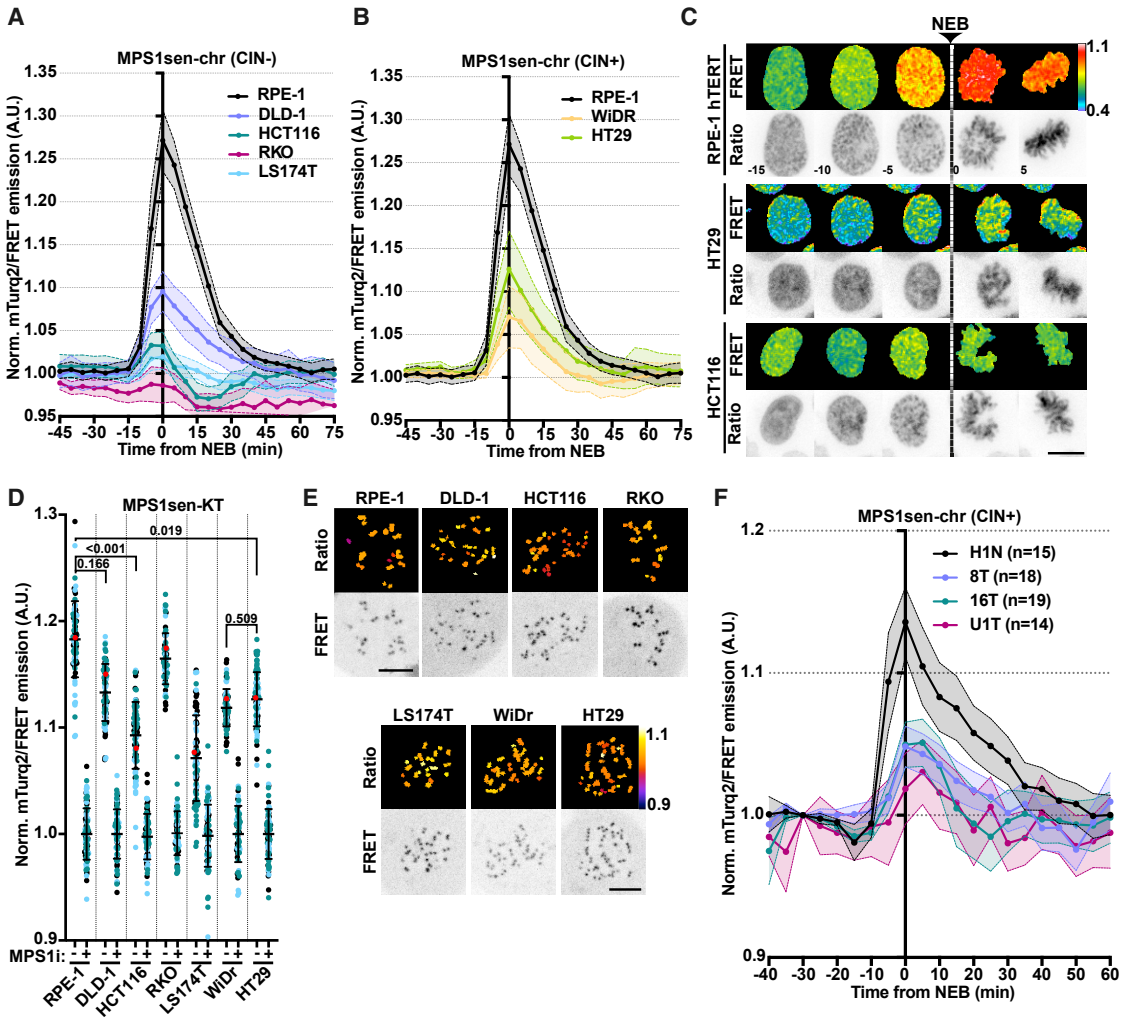

Figure 4. MPS1 Activity Is Deregulated in CRC Cells and Patient-Derived Organoids

(A and B) Quantifications of FRET ratios (mean ± 95% CI) of CRC cell lines and RPE-1 cells (N = 3) stably expressing MPS1sen-chr ("Opti" version, see STAR Methods), synchronized by thymidine (16 h) and released (7 h) before imaging mitotic progression. Cell lines in (A) are classified as CIN-negative (CIN^-) (all N = 2, except HCT116 N = 3), and cell lines in (B) are CIN-positive (CIN^+) (HT29 N = 3, WiDR N = 2). RPE-1 data are same in both graphs. Ratios were normalized on population average of each cell line at t = −51 min.

(C) Images (mTurq2/FRET ratio and FRET channel with real ratio values indicated) of RPE-1, HT29, and HCT116 cells expressing MPS1sen (from data presented in A and B), scaled identically for direct comparison, scale bar, 10 μm.

(D) Quantification of kinetochore-MPS1 activity (MPS1i or solvent [DMSO]) in CRC cells expressing MPS1sen-KT; the process was as described for Figure 1B.

(E) Representative images of data shown in (D); all images were scaled identically for comparison; scale bar, 10 μm.

(F) Quantifications of FRET ratios (mean ± SEM, N ≥ 2) of patient-derived CRC organoids (PDOs) expressing MPS1sen-chr. Organoids were imaged every 5 min for 16 h, and data were normalized at t = −30 min before NEB.

See also Videos S3 and S4 and Figure S4.

in promoting MPS1 activity [21, 49], we next treated cells with the Aurora B inhibitor ZM447439. Inhibition of Aurora B appeared to reduce the speed of MPS1sen-chr phosphorylation, but this was not a significant effect (hillslope DMSO = 0.2440 versus AurBi = 0.2161, p = 0.7209) (Figures 3C ad 3G). Maximum phosphorylation at NEB was substantially reduced, however. MPS1 activity in prometaphase is directly regulated by PP2A-B56 [6], and this phosphatase may also indirectly affect MPS1 activity through regulation of Aurora B [50–52]. We therefore next assessed whether PP2A-B56 affects the activation of MPS1 in prophase. Strikingly, RNAi of B56 (all isoforms [50]) not only elevated the extent of MPS1sen-chr phosphorylation during early mitosis but also advanced its onset by up to 15 min (Figures 3D, 3E, 3G, and S3E–S3G). These effects were largely recapitulated by depletion of the PP2A-B56-binding protein BUBR1 (Figures 3C, 3D, and S3E), suggesting a role for this interaction in MPS1 activity regulation. Interestingly, a BUBR1 mutant (ΔGLEBS) unable to localize to kinetochores [53] fully supported normal timing of MPS1sen-chr phosphorylation (Figures 3F and S3H), implying that the regulation of MPS1 activation by BUBR1-B56 occurs outside the context of kinetochores, for example, in the nucleoplasm or at the nuclear envelope. If PP2A-B56 controls onset of

prophase MPS1sen-chr phosphorylation by antagonizing Aurora B, Aurora B inhibition should revert the premature MSP1sen-chr phosphorylation upon B56 depletion. Nonetheless, while inhibition of Aurora B partly restored the extent of MPS1sen-chr phosphorylation at NEB in B56-depleted cells, it did not restore normal timing of its initiation in prophase (Figures 3G and S3J). These data show that PP2A-B56 and Aurora B together modulate MPS1 peak activity and suggest that PP2A-B56 regulates MPS1 activation timing independently of Aurora B.

MPS1 Signaling Is Deregulated in Colorectal Cancer Cultures

Our data showed that MPS1sen is a specific biosensor for MPS1 kinase activity capable of detecting relatively subtle changes to MPS1 activity dynamics. Cancer cells are marked by extensive aneuploidies that are caused by chromosomal instability (CIN) [54, 55]. The molecular causes for CIN are likely related to pathways generating, regulating, or monitoring correct attachments of kinetochores to spindle microtubules [56, 57]. Since MPS1 is at the heart of these processes, we wished to explore whether MPS1sen would be useful to assess whether alterations to its signaling output are apparent in cancer cells. We selected a panel of colorectal cancer (CRC) cell lines in which aneuploidy levels and CIN status have been extensively documented [58–60] and expressed MPS1sen-chr and MPS1sen-KT by lentiviral transduction. All but one of the CRC cell lines showed reduced MPS1sen phosphorylation on both chromatin and kinetochores compared to non-cancerous RPE-1 cells (Figures 4A–4C and S4A), which could not be explained by differences in MPS1 levels at kinetochores (Figure S4B). The exception, the RKO line, had substantial phosphorylation of MPS1sen at kinetochores but hardly any at chromatin, potentially reflecting diverse local kinase/phosphatase balances compared to the other lines (Figures 4D and 4E). No obvious differences were observed between lines designated as CIN (high aneuploidy) or MSI/MIN (low aneuploidy) (Figures 4A–4C), but other distinctions nonetheless existed: whereas MPS1sen phosphorylation was clearly detectable (albeit low) in some lines (DLD-1, WiDR, HT29), it was very weak in others (LS174T, HCT116). The relative differences in MPS1sen phosphorylation were recapitulated by MPS1 substrate phosphorylation status (MPS1-pT33/37 and KNL1-pMELT) as determined by immuno-imaging (Figures S4C–S4F). It thus seems that attenuated MPS1 signaling is a shared feature of this panel of cancer lines but that it does not correlate with aneuploidy status. To further validate this, we sought to extend our observations to patient-derived stem cell cultures (organoids) that were recently isolated from patients [61, 62]. These tumor organoids closely resemble the tumor of origin and were extensively characterized for CIN status [61, 62]. We introduced MPS1sen-chr into four lines: two non-hypermutated lines with medium CIN, a hypermutated/MSI line with medium CIN, and one normal line derived from healthy colon tissue [62]. Strikingly, while MPS1sen-chr phosphorylation was robust in healthy colon organoids, it was substantially weaker in all tumor lines (Figures 4F and S4G; Videos S3 and S4). Our data therefore suggest that MPS1 signaling is impaired in CRC cells, regardless of the extent of their karyotype aberrations. An important topic for future studies is to examine the causes and consequences of MPS1 activity deregulation in CRC.

STAR★METHODS

Detailed methods are provided in the online version of this paper and include the following:

- KEY RESOURCES TABLE
- RESOURCE AVAILABILITY
  - Lead Contact
  - Materials Availability
  - Data and Code Availability
- EXPERIMENTAL MODEL AND SUBJECT DETAILS
  - Human Cell Lines
  - Patient Derived Organoids
  - Bacterial strains
- METHOD DETAILS
  - Plasmids and molecular cloning
  - Generating stable cell lines & FACS sorting
  - Chemical inhibitors and reagents
  - Oligonucleotides
  - siRNA-mediated knockdown and inducible Cas9 knockout
  - Cell cycle manipulation & protein addback
  - Antibodies
  - Live cell imaging
  - Immunofluorescence
- QUANTIFICATION AND STATISTICAL ANALYSIS

SUPPLEMENTAL INFORMATION

Supplemental Information can be found online at https://doi.org/10.1016/j.cub.2020.07.062.

ACKNOWLEDGMENTS

We thank M. Lampson (University of Pennsylvania) for sharing reagents and MATLAB code, and I. Cheeseman (Whitehead Institute), S. Lens (UMC Utrecht), and H. Snippert (UMC Utrecht) for sharing reagents. We thank S. Sonneveld (Hubrecht Institute) for providing MATLAB code to run analysis in batch mode. We are grateful to members of the Lens, Saurin (Dundee University) and Kops labs for fruitful discussions. The Kops lab is a member of the Oncode Institute, which is partly financed by the Dutch Cancer Society. This study was financially supported by the Netherlands Organization for Scientific Research (NWO/ALWOP.153).

AUTHOR CONTRIBUTIONS

T.E.F.K. and G.J.P.L.K. conceived the project. T.E.F.K. and G.J.P.L.K. designed all experiments. T.E.F.K.., M.L.A.L., and S.W. performed and analyzed experiments. A.C.F.B. performed organoid culturing and selection. D.H.M.S. contributed to validating the first generations of MPS1sen. S.W. generated reagents used in this study. B.P. provided analysis reagent. T.E.F.K. and G.J.P.L.K. wrote the manuscript.

DECLARATION OF INTERESTS

A patent application has been filed by Stichting Oncode Institute for the technology disclosed in this publication.

Received: November 27, 2019
Revised: June 18, 2020
Accepted: July 14, 2020
Published: September 3, 2020

REFERENCES

1. Tanaka, T.U. (2008). Bi-orienting chromosomes: acrobatics on the mitotic spindle. Chromosoma *117*, 521–533.
2. Sacristan, C., and Kops, G.J. (2015). Joined at the hip: kinetochores, microtubules, and spindle assembly checkpoint signaling. Trends Cell Biol. *25*, 21–28.
3. London, N., and Biggins, S. (2014). Signalling dynamics in the spindle checkpoint response. Nat. Rev. Mol. Cell Biol. *15*, 736–747.
4. Pachis, S.T., and Kops, G.J.P.L. (2018). Leader of the SAC: molecular mechanisms of Mps1/TTK regulation in mitosis. Open Biol. *8*, 180109.
5. Jelluma, N., Dansen, T.B., Sliedrecht, T., Kwiatkowski, N.P., and Kops, G.J. (2010). Release of Mps1 from kinetochores is crucial for timely anaphase onset. J. Cell Biol. *191*, 281–290.
6. Hayward, D., Bancroft, J., Mangat, D., Alfonso-Pérez, T., Dugdale, S., McCarthy, J., Barr, F.A., and Gruneberg, U. (2019). Checkpoint signaling and error correction require regulation of the MPS1 T-loop by PP2A-B56. J. Cell Biol. *218*, 3188–3199.
7. Liu, D., Vader, G., Vromans, M.J., Lampson, M.A., and Lens, S.M. (2009). Sensing chromosome bi-orientation by spatial separation of aurora B kinase from kinetochore substrates. Science *323*, 1350–1353.
8. Zaytsev, A.V., Segura-Peña, D., Godzi, M., Calderon, A., Ballister, E.R., Stamatov, R., Mayo, A.M., Peterson, L., Black, B.E., Ataullakhanov, F.I., et al. (2016). Bistability of a coupled Aurora B kinase-phosphatase system in cell division. eLife *5*, e10644.
9. Liu, D., Davydenko, O., and Lampson, M.A. (2012). Polo-like kinase-1 regulates kinetochore-microtubule dynamics and spindle checkpoint silencing. J. Cell Biol. *198*, 491–499.
10. Macůrek, L., Lindqvist, A., Lim, D., Lampson, M.A., Klompmaker, R., Freire, R., Clouin, C., Taylor, S.S., Yaffe, M.B., and Medema, R.H. (2008). Polo-like kinase-1 is activated by aurora A to promote checkpoint recovery. Nature *455*, 119–123.
11. Bruinsma, W., Macurek, L., Freire, R., Lindqvist, A., and Medema, R.H. (2014). Bora and Aurora-A continue to activate Plk1 in mitosis. J. Cell Sci. *127*, 801–811.
12. Alexander, J., Lim, D., Joughin, B.A., Hegemann, B., Hutchins, J.R., Ehrenberger, T., Ivins, F., Sessa, F., Hudecz, O., Nigg, E.A., et al. (2011). Spatial exclusivity combined with positive and negative selection of phosphorylation motifs is the basis for context-dependent mitotic signaling. Sci. Signal. *4*, ra42.
13. Dou, Z., von Schubert, C., Körner, R., Santamaria, A., Elowe, S., and Nigg, E.A. (2011). Quantitative mass spectrometry analysis reveals similar substrate consensus motif for human Mps1 kinase and Plk1. PLoS ONE *6*, e18793.
14. Kemmler, S., Stach, M., Knapp, M., Ortiz, J., Pfannstiel, J., Ruppert, T., and Lechner, J. (2009). Mimicking Ndc80 phosphorylation triggers spindle assembly checkpoint signalling. EMBO J. *28*, 1099–1110.
15. Hiruma, Y., Sacristan, C., Pachis, S.T., Adamopoulos, A., Kuijt, T., Ubbink, M., von Castelmur, E., Perrakis, A., and Kops, G.J.P.L. (2015). CELL DIVISION CYCLE. Competition between MPS1 and microtubules at kinetochores regulates spindle checkpoint signaling. Science *348*, 1264–1267.
16. Ji, Z., Gao, H., and Yu, H. (2015). CELL DIVISION CYCLE. Kinetochore attachment sensed by competitive Mps1 and microtubule binding to Ndc80C. Science *348*, 1260–1264.
17. Koch, A., Maia, A., Janssen, A., and Medema, R.H. (2016). Molecular basis underlying resistance to Mps1/TTK inhibitors. Oncogene *35*, 2518–2528.
18. Hennrich, M.L., Marino, F., Groenewold, V., Kops, G.J., Mohammed, S., and Heck, A.J. (2013). Universal quantitative kinase assay based on diagonal SCX chromatography and stable isotope dimethyl labeling provides high-definition kinase consensus motifs for PKA and human Mps1. J. Proteome Res. *12*, 2214–2224.
19. Lénárt, P., Petronczki, M., Steegmaier, M., Di Fiore, B., Lipp, J.J., Hoffmann, M., Rettig, W.J., Kraut, N., and Peters, J.M. (2007). The small-molecule inhibitor BI 2536 reveals novel insights into mitotic roles of polo-like kinase 1. Curr. Biol. *17*, 304–315.
20. Ditchfield, C., Johnson, V.L., Tighe, A., Ellston, R., Haworth, C., Johnson, T., Mortlock, A., Keen, N., and Taylor, S.S. (2003). Aurora B couples chromosome alignment with anaphase by targeting BubR1, Mad2, and Cenp-E to kinetochores. J. Cell Biol. *161*, 267–280.
21. Saurin, A.T., van der Waal, M.S., Medema, R.H., Lens, S.M., and Kops, G.J. (2011). Aurora B potentiates Mps1 activation to ensure rapid checkpoint establishment at the onset of mitosis. Nat. Commun. *2*, 316.
22. Nijenhuis, W., von Castelmur, E., Littler, D., De Marco, V., Tromer, E., Vleugel, M., van Osch, M.H., Snel, B., Perrakis, A., and Kops, G.J. (2013). A TPR domain-containing N-terminal module of MPS1 is required for its kinetochore localization by Aurora B. J. Cell Biol. *201*, 217–231.
23. Santaguida, S., Vernieri, C., Villa, F., Ciliberto, A., and Musacchio, A. (2011). Evidence that Aurora B is implicated in spindle checkpoint signalling independently of error correction. EMBO J. *30*, 1508–1519.
24. Jelluma, N., Brenkman, A.B., van den Broek, N.J., Cruijsen, C.W., van Osch, M.H., Lens, S.M., Medema, R.H., and Kops, G.J. (2008). Mps1 phosphorylates Borealin to control Aurora B activity and chromosome alignment. Cell *132*, 233–246.
25. Kagami, Y., Nihira, K., Wada, S., Ono, M., Honda, M., and Yoshida, K. (2014). Mps1 phosphorylation of condensin II controls chromosome condensation at the onset of mitosis. J. Cell Biol. *205*, 781–790.
26. McKinley, K.L., Sekulic, N., Guo, L.Y., Tsinman, T., Black, B.E., and Cheeseman, I.M. (2015). The CENP-L-N Complex Forms a Critical Node in an Integrated Meshwork of Interactions at the Centromere-Kinetochore Interface. Mol. Cell *60*, 886–898.
27. Rodriguez-Bravo, V., Maciejowski, J., Corona, J., Buch, H.K., Collin, P., Kanemaki, M.T., Shah, J.V., and Jallepalli, P.V. (2014). Nuclear pores protect genome integrity by assembling a premitotic and Mad1-dependent anaphase inhibitor. Cell *156*, 1017–1031.
28. Ji, Z., Gao, H., Jia, L., Li, B., and Yu, H. (2017). A sequential multi-target Mps1 phosphorylation cascade promotes spindle checkpoint signaling. eLife *6*, e22513.
29. Cunha-Silva, S., Osswald, M., Goemann, J., Barbosa, J., Santos, L.M., Resende, P., Bange, T., Ferrás, C., Sunkel, C.E., and Conde, C. (2020). Mps1-mediated release of Mad1 from nuclear pores ensures the fidelity of chromosome segregation. J. Cell Biol. *2*, e201906039.
30. Etemad, B., Kuijt, T.E.F., and Kops, G.J.P.L. (2015). Kinetochore-microtubule attachment is sufficient to satisfy the human spindle assembly checkpoint. Nat. Commun. *6*, 8987.
31. Tauchman, E.C., Boehm, F.J., and DeLuca, J.G. (2015). Stable kinetochore-microtubule attachment is sufficient to silence the spindle assembly checkpoint in human cells. Nat. Commun. *6*, 10036.
32. Dou, Z., Liu, X., Wang, W., Zhu, T., Wang, X., Xu, L., Abrieu, A., Fu, C., Hill, D.L., and Yao, X. (2015). Dynamic localization of Mps1 kinase to kinetochores is essential for accurate spindle microtubule attachment. Proc. Natl. Acad. Sci. USA *112*, E4546–E4555.
33. Etemad, B., Vertesy, A., Kuijt, T.E.F., Sacristan, C., van Oudenaarden, A., and Kops, G.J.P.L. (2019). Spindle checkpoint silencing at kinetochores with submaximal microtubule occupancy. J. Cell Sci. *132*, jcs231589.
34. von Schubert, C., Cubizolles, F., Bracher, J.M., Sliedrecht, T., Kops, G.J.P.L., and Nigg, E.A. (2015). Plk1 and Mps1 Cooperatively Regulate the Spindle Assembly Checkpoint in Human Cells. Cell Rep. *12*, 66–78.
35. Ballister, E.R., Riegman, M., and Lampson, M.A. (2014). Recruitment of Mad1 to metaphase kinetochores is sufficient to reactivate the mitotic checkpoint. J. Cell Biol. *204*, 901–908.
36. Kuijt, T.E.F., Omerzu, M., Saurin, A.T., and Kops, G.J.P.L. (2014). Conditional targeting of MAD1 to kinetochores is sufficient to reactivate the spindle assembly checkpoint in metaphase. Chromosoma *123*, 471–480.
37. Maldonado, M., and Kapoor, T.M. (2011). Constitutive Mad1 targeting to kinetochores uncouples checkpoint signalling from chromosome bi-orientation. Nat. Cell Biol. *13*, 475–482.

38. Williams, S.J., Abrieu, A., and Losada, A. (2017). Bub1 targeting to centromeres is sufficient for Sgo1 recruitment in the absence of kinetochores. Chromosoma *126*, 279–286.

39. El Yakoubi, W., Buffin, E., Cladière, D., Gryaznova, Y., Berenguer, I., Touati, S.A., Gómez, R., Suja, J.A., van Deursen, J.M., and Wassmann, K. (2017). Mps1 kinase-dependent Sgo2 centromere localisation mediates cohesin protection in mouse oocyte meiosis I. Nat. Commun. *8*, 694.

40. Wood, K.W., Lad, L., Luo, L., Qian, X., Knight, S.D., Nevins, N., Brejc, K., Sutton, D., Gilmartin, A.G., Chua, P.R., et al. (2010). Antitumor activity of an allosteric inhibitor of centromere-associated protein-E. Proc. Natl. Acad. Sci. USA *107*, 5839–5844.

41. Barisic, M., Aguiar, P., Geley, S., and Maiato, H. (2014). Kinetochore motors drive congression of peripheral polar chromosomes by overcoming random arm-ejection forces. Nat. Cell Biol. *16*, 1249–1256.

42. Ikeda, M., and Tanaka, K. (2017). Plk1 bound to Bub1 contributes to spindle assembly checkpoint activity during mitosis. Sci. Rep. *7*, 8794.

43. Gavet, O., and Pines, J. (2010). Activation of cyclin B1-Cdk1 synchronizes events in the nucleus and the cytoplasm at mitosis. J. Cell Biol. *189*, 247–259.

44. Mills, G.B., Schmandt, R., McGill, M., Amendola, A., Hill, M., Jacobs, K., May, C., Rodricks, A.M., Campbell, S., and Hogg, D. (1992). Expression of TTK, a novel human protein kinase, is associated with cell proliferation. J. Biol. Chem. *267*, 16000–16006.

45. Alfonso-Pérez, T., Hayward, D., Holder, J., Gruneberg, U., and Barr, F.A. (2019). MAD1-dependent recruitment of CDK1-CCNB1 to kinetochores promotes spindle checkpoint signaling. J. Cell Biol. *218*, 1108–1117.

46. Cheeseman, I.M., and Desai, A. (2008). Molecular architecture of the kinetochore-microtubule interface. Nat. Rev. Mol. Cell Biol. *9*, 33–46.

47. Hayward, D., Alfonso-Pérez, T., Cundell, M.J., Hopkins, M., Holder, J., Bancroft, J., Hutter, L.H., Novak, B., Barr, F.A., and Gruneberg, U. (2019). CDK1-CCNB1 creates a spindle checkpoint-permissive state by enabling MPS1 kinetochore localization. J. Cell Biol. *218*, 1182–1199.

48. D'Angiolella, V., Mari, C., Nocera, D., Rametti, L., and Grieco, D. (2003). The spindle checkpoint requires cyclin-dependent kinase activity. Genes Dev. *17*, 2520–2525.

49. Santaguida, S., Tighe, A., D'Alise, A.M., Taylor, S.S., and Musacchio, A. (2010). Dissecting the role of MPS1 in chromosome biorientation and the spindle checkpoint through the small molecule inhibitor reversine. J. Cell Biol. *190*, 73–87.

50. Foley, E.A., Maldonado, M., and Kapoor, T.M. (2011). Formation of stable attachments between kinetochores and microtubules depends on the B56-PP2A phosphatase. Nat. Cell Biol. *13*, 1265–1271.

51. Meppelink, A., Kabeche, L., Vromans, M.J., Compton, D.A., and Lens, S.M. (2015). Shugoshin-1 balances Aurora B kinase activity via PP2A to promote chromosome bi-orientation. Cell Rep. *11*, 508–515.

52. Nijenhuis, W., Vallardi, G., Teixeira, A., Kops, G.J., and Saurin, A.T. (2014). Negative feedback at kinetochores underlies a responsive spindle checkpoint signal. Nat. Cell Biol. *16*, 1257–1264.

53. Taylor, S.S., Ha, E., and McKeon, F. (1998). The human homologue of Bub3 is required for kinetochore localization of Bub1 and a Mad3/Bub1-related protein kinase. J. Cell Biol. *142*, 1–11.

54. Duijf, P.H., and Benezra, R. (2013). The cancer biology of whole-chromosome instability. Oncogene *32*, 4727–4736.

55. Bakhoum, S.F., and Compton, D.A. (2012). Chromosomal instability and cancer: a complex relationship with therapeutic potential. J. Clin. Invest. *122*, 1138–1143.

56. Holland, A.J., and Cleveland, D.W. (2012). Losing balance: the origin and impact of aneuploidy in cancer. EMBO Rep. *13*, 501–514.

57. Thompson, S.L., Bakhoum, S.F., and Compton, D.A. (2010). Mechanisms of chromosomal instability. Curr. Biol. *20*, R285–R295.

58. Berg, K.C.G., Eide, P.W., Eilertsen, I.A., Johannessen, B., Bruun, J., Danielsen, S.A., Bjørnslett, M., Meza-Zepeda, L.A., Eknæs, M., Lind, G.E., et al. (2017). Multi-omics of 34 colorectal cancer cell lines - a resource for biomedical studies. Mol. Cancer *16*, 116.

59. Thompson, S.L., and Compton, D.A. (2008). Examining the link between chromosomal instability and aneuploidy in human cells. J. Cell Biol. *180*, 665–672.

60. Lengauer, C., Kinzler, K.W., and Vogelstein, B. (1997). Genetic instability in colorectal cancers. Nature *386*, 623–627.

61. van de Wetering, M., Francies, H.E., Francis, J.M., Bounova, G., Iorio, F., Pronk, A., van Houdt, W., van Gorp, J., Taylor-Weiner, A., Kester, L., et al. (2015). Prospective derivation of a living organoid biobank of colorectal cancer patients. Cell *161*, 933–945.

62. Bolhaqueiro, A.C.F., Ponsioen, B., Bakker, B., Klaasen, S.J., Kucukkose, E., van Jaarsveld, R.H., Vivié, J., Verlaan-Klink, I., Hami, N., Spierings, D.C.J., et al. (2019). Ongoing chromosomal instability and karyotype evolution in human colorectal cancer organoids. Nat. Genet. *51*, 824–834.

63. Vleugel, M., Tromer, E., Omerzu, M., Groenewold, V., Nijenhuis, W., Snel, B., and Kops, G.J. (2013). Arrayed BUB recruitment modules in the kinetochore scaffold KNL1 promote accurate chromosome segregation. J. Cell Biol. *203*, 943–955.

64. Suijkerbuijk, S.J., van Osch, M.H., Bos, F.L., Hanks, S., Rahman, N., and Kops, G.J. (2010). Molecular causes for BUBR1 dysfunction in the human cancer predisposition syndrome mosaic variegated aneuploidy. Cancer Res. *70*, 4891–4900.

65. Arbab, M., Srinivasan, S., Hashimoto, T., Geijsen, N., and Sherwood, R.I. (2015). Cloning-free CRISPR. Stem Cell Reports *5*, 908–917.

66. Schindelin, J., Arganda-Carreras, I., Frise, E., Kaynig, V., Longair, M., Pietzsch, T., Preibisch, S., Rueden, C., Saalfeld, S., Schmid, B., et al. (2012). Fiji: an open-source platform for biological-image analysis. Nat. Methods *9*, 676–682.

67. Fuller, B.G., Lampson, M.A., Foley, E.A., Rosasco-Nitcher, S., Le, K.V., Tobelmann, P., Brautigan, D.L., Stukenberg, P.T., and Kapoor, T.M. (2008). Midzone activation of aurora B in anaphase produces an intracellular phosphorylation gradient. Nature *453*, 1132–1136.

68. Drost, J., van Jaarsveld, R.H., Ponsioen, B., Zimberlin, C., van Boxtel, R., Buijs, A., Sachs, N., Overmeer, R.M., Offerhaus, G.J., Begthel, H., et al. (2015). Sequential cancer mutations in cultured human intestinal stem cells. Nature *521*, 43–47.

69. Adriaans, I.E., Basant, A., Ponsioen, B., Glotzer, M., and Lens, S.M.A. (2019). PLK1 plays dual roles in centralspindlin regulation during cytokinesis. J. Cell Biol. *218*, 1250–1264.

STAR★METHODS

KEY RESOURCES TABLE

REAGENT or RESOURCE	SOURCE	IDENTIFIER
Antibodies		
Mouse anti CENP-A	Abcam	(Cat# ab13939, RRID: AB_300766)
guinea pig anti-CENP-C	MBL International	Cat# PD030; RRID: AB_10693556
rabbit anti-KNL1-pT943/1155 (custom polyclonal serum)	N/A	[63]
rabbit anti-BUB1	Bethyl	Cat# A300-373 A-1; RRID: AB_2065943
mouse anti-HEC1 (9G3.23)	Thermo Fisher Scientific	Cat# MA1-23308; RRID: AB_2149871
mouse anti-MPS1-NT (clone 3-472-1)	Millipore	Cat# 05-682; RRID: AB_11214479
rabbit anti-MPS1-pT33/S37 (phospho-TTK Thr33/Ser37)	Thermo Fisher Scientific	Cat# 44-1325G; RRID: AB_2533594
rabbit anti BUBR1	Bethyl	Cat# A300-995A, RRID:AB_2066087
goat anti-guinea pig Alexa Fluor 647	Molecular Probes	Cat# A21450; RRID: AB_141882
goat anti-rabbit Alexa Fluor 488	Molecular Probes	Cat# A11034; RRID: AB_142134
goat anti-rabbit Alexa Fluor 568	Molecular Probes	Cat# A11036; RRID: AB_143011
goat anti-mouse Alexa Fluor 488	Molecular Probes	Cat# A11029; RRID: AB_138404
goat anti-mouse Alexa Fluor 568	Molecular Probes	Cat# A11031; RRID: AB_144696
goat anti-mouse Alexa Fluor 647	Molecular Probes	Cat# A21240; RRID: AB_2535809
goat anti-guinea pig Alexa Fluor 568	Molecular Probes	Cat# A11075; RRID: AB_2534119
Bacterial and Virus Strains		
E. coli Stbl3	Thermo Fisher Scientific	C737303
Lentivirus pLV-CMV-MCS_IRES-PURO	This study	[62]
Biological Samples		
Colon PDO – H1N	Hubrecht Organoid Technology (HUB) Foundation	Hub-colon-003 [62]
Colon PDO – 8T	Hubrecht Organoid Technology (HUB) Foundation	P8T-O [62]
Colon PDO –16T	Hubrecht Organoid Technology (HUB) Foundation	P16T-O [62]
Colon PDO – U1T (CRC29 UMC nomenclature)	Hubrecht Organoid Technology (HUB) Foundation	U1T [62]
Chemicals, Peptides, and Recombinant Proteins		
Nocodazole	Sigma-Aldrich	Cat# M1404
STLC	Tocris Bioscience	Cat# 1291
Rutin	Thermo Fisher Scientific	Cat# AC132391000
Cpd-5 (MPS1 inhibitor)	Custom	[17]
ZM-447439 (Aurora B inhibitor)	Tocris Bioscience	Cat# 2458
BI-2536	AChemBlock	Cat# 10293
MG-132 (proteasome inhibitor)	Sigma-Aldrich	Cat# C2211
RO-3306 (CDK1 inhibitor)	Tocris Bioscience	Cat# 4181
GSK923295 (CENP-E inhibitor)	Selleck Chem	Cat# S7090
ProTAME (E3-ubiquitin ligase inhibitor)	Boston Chemicals	Cat# I-440
Puromycin	Sigma-Aldrich	Cat# P7255
Blasticidin	Invivogen	Cat# ant-bl-05
Hygromycin B	Sigma-Aldrich	Cat# 10843555001
Doxycycline	Sigma-Aldrich	Cat# D9891
Thymidine	Sigma-Aldrich	Cat# T1895

(*Continued on next page*)

Continued

REAGENT or RESOURCE	SOURCE	IDENTIFIER
Y-27632 (Rock Inhibitor)	Sigma-Aldrich	Y-27632
Experimental Models: Cell Lines		
HeLa FLPin T-Rex	Gift from S. Taylor lab (University of Manchester)	N/A
HeLa FLPin T-Rex – HA-mCherry-BUB1 knockin	N/A	[33]
RPE-1 FLPin hTERT	Gift from J. Pines lab (The Institute of Cancer Research)	N/A
DLD-1	Hubrecht	N/A
HCT-116	Hubrecht	N/A
HT29	Hubrecht	N/A
LS174T	Hubrecht	N/A
RKO	Hubrecht	N/A
WiDr	Hubrecht	N/A
Oligonucleotides		
siRNA targeting sequence: GAPDH	Dharmacon	D-001830-01-05
siRNA targeting sequence: MPS1 (custom): GACAGAUGAUUCAGUUGUA	Dharmacon	[24]
siRNA targeting sequence: HEC1-UTR: CCCUGGGUCGUGUCAGGAA	Dharmacon	[30]
siRNA targeting sequence: BUBR1-UTR: GUCUCACAGAUUGCUGCCU	Dharmacon	[64]
siRNA targeting sequence: B56 (pool)	Dharmacon	[50]
α: UGAAUGAACUGGUUGAGUA		
β: GAACAAUGAGUAUAUCCUA		
γ: UGACUGAGCCGGUAAUUGU		
δ: GGAAGAUGAACCAACGUUA		
E: GCACAGCUGGCAUAUUGUA		
siRNA targeting sequence: MAD2 (custom) GUCUCACAGAUUGCUGCCU	Dharmacon	[52]
BUBR1-E409K site-directed mutagenesis primers	This study	N/A
Sense: gaagatttatgcaggagtagggaaattctcctttgaagaaattcgg, antisense: ccgaatttcttcaaaggagaatttccctactcctgcataaatcttc		
Recombinant DNA		
pOG44 Flp-Recombinase expression vector	Invitrogen	Cat# V600520
pcDNA3-mTurq2-MPS1sen-chr	This study	N/A
pcDNA3-mTurq2-MPS1sen-KT	This study	N/A
pcDNA3-mTurq2-MPS1sen-centr	This study	N/A
pcDNA3-mTurq2-MPS1sen	This study	N/A
pcDNA3-mTurq2-MPS1sen-Ala-chr	This study	N/A
pcDNA3-mTurq2-MPS1sen-chr_P2A-mScarlet-NLS	This study	N/A
pcDNA3-mTurq2-MPS1sen_P2A-mScarlet-NLS	This study	N/A
pcDNA5-mCherry-BUBR1-WT	This study	N/A
pcDNA5-mCherry-BUBR1-E409K	This study	N/A
pLV-mTurq2-MPS1sen-Opti-chr	This study	N/A
pLV-mTurq2-MPS1sen-Opti-KT	This study	N/A
pLV-mTurq2-MPS1sen-Opti-centr	This study	N/A
pcDNA3-spCas9-IRES-PURO	[33]	N/A

(*Continued on next page*)

Continued

REAGENT or RESOURCE	SOURCE	IDENTIFIER
sgPal7-HygR	[65]	Addgene #71484
Software and Algorithms		
GraphPad Prism 8.2.1	GraphPad	https://www.graphpad.com/scientific-software/prism/
Fiji build 1.52p	[66]	https://imagej.nih.gov/ij/
MATLAB 2012b	Mathworks	www.mathworks.com
Imaris XT 9.3.1	Bitplate	www.bitplate.com
XT Mean Intensity Ratio plugin (customized)	Ben	open.bitplane.com
MATLAB_FRET_KT quantification code (customized)	[67]	https://github.com/KOPSlab/Kuijt_etal_2020/releases/tag/V1.0
KT_ImmunoQuanti_Fiji code (custom)	[21]	https://github.com/KOPSlab/Kuijt_etal_2020/releases/tag/V1.0.0

RESOURCE AVAILABILITY

Lead Contact

Further information and requests for resources and reagents should be directed to and will be fulfilled by the Lead Contact, Geert Kops (g.kops@hubrecht.eu).

Materials Availability

Plasmids have been deposited in Addgene and cell lines generated in this study can be obtained through the Lead Contact.

Data and Code Availability

Code for FRET analysis in Fiji is part of another, ongoing study and will be made available by B. Ponsioen upon its publication. All other scripts have been released on https://github.com/KOPSlab/Kuijt_etal_2020/releases.

EXPERIMENTAL MODEL AND SUBJECT DETAILS

Human Cell Lines

HeLa FLPin T-Rex, HeLa inducible Cas9 (iCas9), WiDR and HT29 cells were cultured in DMEM - high glucose (Thermo Fisher Scientific, 11965092) supplemented with 10% Tet-free fetal bovine serum (Sigma), penicillin-streptomycin (50 μg/ml, Sigma P0781) Ala-Gln (2 mM, Sigma G8541). RPE-1 hTERT FLPin T-Rex and RKO cells were cultured in DMEM/F12 (Thermo Fisher Scientific) + 10% Tet-free FBS, 50 μg/ml pen/strep and 2mM Ala-Gln. DLD-1 and LS174T cells were cultured in RPMI (Thermo Fisher Scientific) supplemented with 10% FBS, 50 μg/ml pen/strep and 2mM Ala-Gln. HCT116 were cultured in McCoy's 5A (Sigma) medium 10% FBS, 50 μg/ml pen/strep and 2mM Ala-Gln. Cell line identity was verified by microscopic inspection of morphological traits as described in literature. All cell lines were cultured at 37°C with 5% CO2.

Patient Derived Organoids

Colon patient-derived organoids (PDOs) were cultured in medium containing advanced DMEM/F12 medium (Invitrogen) supplemented with: 1 mM HEPES buffer (Sigma-Aldrich), 1% (v/v) penicillin/streptomycin (Sigma-Aldrich), 200 μM Ala-Glu (Sigma-Aldrich), 20% (v/v) R-spondin-conditioned medium, 10% (v/v) Noggin-conditioned medium, 1x B27 (Thermo/Life Technologies), 10mM nicotinamide (Sigma-Aldrich), 1.25 mM N-acetylcysteine (Sigma-Aldrich), 500mM A83-01 (Tocris Bioscience), 50ng/ml EGF (Invitrogen/Life Technologies), 3 μM SB203580 (Invitrogen/Life Technologies). For colon PDOs, 50% WNT-conditioned medium (produced using stably transfected L cells) was added. All organoids were cultured at 37°C with 5% CO2. Tumor PDOs were passaging by dissociating with TrypLE (GIBCO) and colon PDOs were mechanically dissociated. The PDOs were then placed in Matrigel in a pre-warmed 24-well plate and upon plating 10μM Rock inhibitor Y-27632 (Sigma-Aldrich) was added to the culture medium for 48 hours. Tumor and colon PDOs expressing MPS1sen-Opti-chr were generated by transducing with lentivirus and subsequent selection with 1μg/μl puromycin for 3 days [68]. PDOs were not subjected to FACS sorting to isolate a specific MPS1sen expressing population. Two days before imaging of PDOs, PDOs were dissociated with TrypLE (Thermo Fisher Scientific) and colon PDOs were mechanically dissociated. The PDOs were plated in Matrigel in a pre-warmed 8-well glass bottom μ-slide (Ibidi, #80827). Upon plating, Rock inhibitor (10 μM, Sigma-Aldrich Y-27632) was added to culture medium for 2 days.

Bacterial strains

Bacterial strain *E. coli* Stbl3 was grown at 37°C in standard LB medium.

METHOD DETAILS

Plasmids and molecular cloning

MPS1sen was generated by restriction digestion of pIRES-PURO-H2B-mTFP1-Aurora B with BamHI/BspEI (NEB). The MPS1sen substrate sequence (or MPS1sen-Ala) was inserted using synthesized DNA oligo's and validated by Sanger sequencing. mTFP1 was replaced by mTurquoise2 (mTurq2, gift from D. Gadella, Addgene plasmid 36202) by PCR and inserted by restriction digestion (NheI/KpnI). The H2B coding sequence was substituted by restriction digestion with AscI/NheI and PCR amplification of CENP-B (DNA binding domain, 1-158) to generate MPS1sen-cent. N-terminal fusions to MPS1sen were generated by subcloning of a plasmid containing mTFP1-Aurora B-YPet-CAAX [69] (gift from S. Lens) where mTFP1 was replaced by mTurq2 and a multiple cloning site identical to the MCS found in plasmid pDL009-HEC1-Aurora B biosensor (gift from M. Lampson, Addgene plasmid 45239) was inserted. SPC24 coding region was PCR amplified from cDNA to create MPS1sen-KT. To visualize nuclear envelope breakdown, mScarlet (gift from D. Gadella, Addgene plasmid 85054) was amplified by PCR, adding an N-terminal P2A sequence and a C-terminal SV40-NLS sequence. This fragment was inserted by Gibson assembly cloning behind the IRES-PURO of various MPS1sen-plasmids. The mCherry-BUBR1-WT and ΔGLEBS mutants were generated by PCR amplification of BUBR1 cDNA and subsequent Gibson assembly into a pcDNA5-mCherry backbone. Site-directed mutagenesis followed by sanger sequencing was performed to introduce the E409K mutation.

To generate lentivirus MPS1sen versions, pLV-H2B-mNeon_IRES-PURO [68] was digested with AscI/NheI and backbone was gel purified. MPS1sen was PCR-amplified and inserted by Gibson assembly cloning. mTurq2 was replaced with a codon-optimized version of Turquoise2GL (kind gift from H. Snippert) to prevent recombination of MPS1sen during production of lentivirus. To reduce Turq2-YPet dimerization, the K206A and V224L 'sticky'-mutations in Turquoise2GL were reverted by site-directed mutagenesis, generating MPS1sen-Opti. Lentiviral constructs CENP-B (MPS1sen-Opti-cent) and SPC24 (MPS1sen-Opti-kt), were generated by Gibson assembly. Coding regions of all MPS1sen-Opti plasmids were verified by Sanger sequencing.

Generating stable cell lines & FACS sorting

To generate HeLa cells expressing MPS1sen, plasmids were transfected using Fugene HD (Roche) according to manufactures instruction and 24 hr. after transfection puromycin was added. RPE-1, HeLa iCas9 and CRC cell lines were generated by transduction with lentiviral MPS1sen-Opti. After growing out stable clones expressing MPS1sen(-Opti), cells were FACS sorted to isolate a polyclonal population that expressed mTurq2:YPet at 1:1 ratio. Cells were resuspended after trypsin in DMEM, pelleted at 300xg for 3 min. by centrifugation, washed with 1xPBS0 (-Mg^{2+}/Ca^{2+}) and resuspended in FACS buffer (1xPBS0 + 25mM HEPES pH7.2 + 0.1% EDTA + 0.1% FCS). FACS sorting was performed on a custom BD FACSAria Fusion flow cytometer system. mTurq2 (Ex405nm, Em450/50) was plotted against YPet (Ex488nm, Em549/15) and mScarlet/mCherry (Ex561nm, Em610/20) against autofluorescence (Ex640nm, Em670/30). Sorted cells were collected in cooled DMEM full growth medium (FGM) supplemented with 10% FBS and 10mM HEPES (Sigma).

HeLa FLP-in TRex cell lines were generated as described previously [22]. In brief, 1x10^6 cells were reverse transfected using Fugene HD with 4.5 μg pOG44 and 0.5μg pcDNA5 donor plasmid. Clones were selected by addition of 500μg/ml hygromycin B (Roche) for 5 days. Endogenously tagged HA-mCherry-BUB1 HeLa FLPin T-Rex cell line was described previously [33]. In brief, HeLa cells were transfected with plasmid sgPal7-HygR, spCas9-IRES-Puro [65] and 1 μg linear PCR fragments of sgRNA targeting BUB1 locus and homology template encoding HA-mCherry. Transfected cells were selected using 500 μg/ml hygromycin B and 1 μg/ml puromycin for 48 hours. Single cell clones were isolated by FACS sorting.

Chemical inhibitors and reagents

The following chemicals were used at indicated final concentrations unless state otherwise in figure legends: nocodazole (6.6 μM, Sigma-Aldrich M1404), MG-132 (5 μM, Sigma-Aldrich C2211), thymidine (200 mM, Sigma-Aldrich T1895), ZM-447439 (2μM, Tocris Bioscience 2458), Cpd-5 (500 nM, MPS1 inhibitor [17]), RO-3306 (8 μM, Tocris Bioscience 4181), STLC (10 μM, Tocris Bioscience 1291), GSK923295 CENP-E inhibitor (250nM, Selleck Chem), proTAME (3.3 μM, Boston Chemicals I-440), puromycin (1μg/ml, Sigma, P7255), Rutin (16 μM, Thermo Fisher Scientific AC132391000).

Oligonucleotides

The following siRNAs were used at 20nM final concentration unless stated otherwise: siGAPD (ON-TARGETplus Dharmacon D-001830-01-05), siMPS1 [24]: GACAGAUGAUUCAGUUGUA, siMAD2 [52]: UACGGACUCACCUUGCUUG, siHEC1-UTR (40nM) [30]: CCCUGGGUCGUGUCAGGAA, Pool of siB56 [50] (50nm): B56α: UGAAUGAACUGGUUGAGUA, B56β: GAACAAUGA GUAUAUCCUA, B56γ: UGACUGAGCCGGUAAUUGU, B56δ: GGAAGAUGAACCAACGUUA, B56E: GCACAGCUGGCAUAUUGUA, siBUBR1-UTR [64] (100nM): GUCUCACAGAUUGCUGCCU.

siRNA-mediated knockdown and inducible Cas9 knockout

Delivery of siRNAs was performed using Lipofectamin RNAiMax (Thermo Fisher Scientific). In brief: cells were plated to 12 well plate in 625μl medium (50% full growth medium + 50% Optimem (Thermo Fisher Scientific). Lipid:siRNA complexed were formed in 123 μl optimem + siRNA and 1.25μl RNAiMax, incubated for 10 min. before addition to cells. siRNA was performed for 36 hr. (siB56) or 48 hr. (siHEC1, siMPS1, siMAD2, siBUBR1).

Induction of Cas9 in conditional HeLa control or CENP-C knockout cell lines was achieved by addition of doxycycline for 96 hours (with fresh doxycycline added every 24 hours).

Cell cycle manipulation & protein addback

Cell synchronization was performed by addition of 2 mM thymidine (Sigma) for 20 hr. and cells were released from thymidine for 7 hr. before performing assays. Arresting cells at G2 was performed by addition of 8 μM RO-3306 for 17 hr. and cells were released from CDK1 blocks by washing 2x with DMEM medium while inside the microscope.

Antibodies

The following primary antibodies were used for immunofluorescence: guinea pig anti-CENP-C (1:2000, MBL Life Science PD030), rabbit anti-KNL1-pT943/1155 ((pMELT), custom described in ref [63].), rabbit anti-BUB1 (1:2000, Bethyl A300-373 A-1), mouse anti-HEC1 (1:1000, Thermo Fisher Scientific MA1-23308), mouse anti-MPS1-NT (1:500, Millipore 05-682), rabbit anti-MPS1-pT33/S37 (1:1000, Thermo Fisher Scientific 44-1325G), mouse anti-CENP-A (1:1000, abcam 13939), rabbit anti BUBR1 (1:1000, Bethyl A300-995A) and secondary antibodies at 1:1000, goat anti-guinea pig Alexa Fluor 647 (Molecular Probes A21450), goat anti-rabbit Alexa Fluor 488 (Molecular Probes A11034), goat anti-rabbit Alexa Fluor 568 (Molecular Probes A11036), goat anti-mouse Alexa Fluor 488 (Molecular Probes A11029), goat anti-mouse Alexa Fluor 568 (Molecular Probes A11031).

Live cell imaging

Cells were plated on 96-well glass bottom 1.5H well plates (CellVis) 24 hr. before imaging. For experiments in which cells were released from G2 by RO-3306 block, medium was replaced by warm DMEM medium twice and image acquisition was initiated directly after or medium replacements were performed in between image acquisition rounds. Live-cell imaging was performed in freshly prepared $DMEM^{gfp}$-2 medium (Evrogen MC102) supplemented with 8% FBS, 2 mM Ala-Gln and 16μM rutin (in DMSO).

Live cell imaging of all cell lines was performed on a Nikon TiE microscope, controlled by NIS Elements software (Nikon v4.56), equipped with a Yokagawa CSU-W1-T2 spinning disk (dual disk), Borealis (Andor), two iXon-888 Ultra EMCCD cameras (Andor), 1x camera relay lens and ILE-400 (Andor) laser emission controller. MPS1sen was excited using a 445nm ± 5nm laser with 35 - 45 μW at the objective, passing emission light through a 445-561-640 custom dichroic mirror to block excitation light and emission light of mTurquoise2 and FRET (YPet) was split by a 514nm dichroic mirror (Semrock). Emission light was collected with 490-40nm (Chroma) and 545-50 (Semrock) emission filters. For experiments involving mScarlet, a 561nm laser (100mW rated) was used at the lowest possible intensity and emission was collected with a 609-57nm filter (Semrock). All imaging was performed using a PLANAPO 100x 1.45 NA objective lens (Nikon) and 50μm pinhole disk. For imaging H2B and cytoplasmic MPS1sen camera settings were: 2x2 binning, 10MHz readout speed, gain 1 mode, −80°C cooled EMCCD, 100-150ms exposure time and 3x6μm Z-steps (12μm stack size). For imaging FRET at kinetochores or centromeres the following settings were used: 1x1 binning, 1MHz readout speed, gain 2 mode, 300 EM-gain (both channels), −90°C cooled EMCCD-chip, 150x150 ROI, 200-300ms exposure and for kinetochore-FRET 2x averaging was applied. Z-steps were 0.6 μm with a 2.4 μm stack size for kinetochores and 7.8 μm stack size for centromere FRET. CENP-E-inhibited cells were imaged with a Z stack of 19 images to capture both aligned and unaligned objects in the cell.

For imaging colon PDO, a 30x UPLSAPO silicone objective lens (Olympus) was mounted on above described spinning disk microscope by using a M25 to RMS adaptor (RMSA1, Thorlabs) and a 15mm parfocal extender (PLE152, Thorlabs).

Immunofluorescence

Cells were plated on glass ø10 mm coverslips (#1.5H) > 24 hr. before fixation. Cells were pre-extracted with 37°C PHEM-TX100 (PIPES, HEPES, EGTA, 2 mM MgCl2, 0.2% Triton X-100) for 1 min. at room temperature after which cells were fixed in freshly prepared 4% paraformaldehyde/PBS (pH7.2) for 5 mins. at room temperature. Cells were washed with PBS and blocked in 3% BSA/PBS (blocking buffer) for 30 min. at room temperature. Primary antibody dilutions were made in blocking buffer and coverslips were incubated at 4°C overnight inverted. Next, cells were washed in blocking buffer + 0.1% Triton X-100 followed by 1 hr. incubation with secondary antibodies diluted in blocking buffer. Coverslips were washed in blocking buffer and a final wash step in ddH2O before mounting onto glass slides using Prolong Gold antifade (Thermo Fisher Scientific). Images were acquired on a DeltaVision Elite (GE Healthcare) with a 100x 1.40NA UPlanSApo objective (Olympus) and SoftWorx 6.0 software (GE Healthcare). Images were acquired with 0.15μm Z-intervals and then deconvolved and maximum intensity projections were made using SoftWorx. Early prometaphase cells were selected based on the shape of DAPI signal.

QUANTIFICATION AND STATISTICAL ANALYSIS

Immunofluorescent images were quantified using Fiji [66] using custom scripts (named: KT-ImmunoQuanti_Fiji). In brief: on a maximum projected image, a region of interest (ROI) was drawn to exclude neighboring cells, followed by applying a threshold to generate an ROI of the DAPI signal, following a threshold on CENP-C channel to generate an ROI for kinetochore signal. The kinetochore ROI was subtracted from the DAPI-ROI and background and kinetochore signals were measured in all channels except DAPI channel. The mean background intensity was subtracted from mean kinetochore signal and the kinetochore/CENP-C ratios were computed.

Time-lapse FRET data from H2B and cytoplasmic MPS1sen were sum projected (in Z axis) using Fiji and analyzed using custom written macro in Fiji (B. Ponsioen, unpublished). In brief, background was subtracted for each channel over time and background was set to NaN using manual set threshold on the weighted sum of donor/acceptor intensities. Next, donor/acceptor ratio image was computed, a region of interest (ROI) was manually placed and a thresholding (weighted sum of donor/acceptor) was applied to define pixels for quantification. The pooled donor/acceptor ratios were computed and used for subsequent data normalization. For H2B FRET cells, normalization was applied at t = −51 min. before full NEB by computing the population average, for data shown in Figure S1H normalization was applied at t = −30 min. For cytoplasmic MPS1sen quantifications a 15x15 pixel ROI was placed in the nucleus or cytoplasm and analyzed as described for H2B data. Data was normalized by setting the first frame to 1 for each cell where the mean FRET ratio of nuclear and cytoplasm was used per cell. Similarly, in mScarlet channel the cytoplasmic/nuclear intensities were quantified in one of three replicate experiments to define the start and completion of NEB.

Raw kinetochore/centromere FRET data was processed using custom written macro in Fiji and MATLAB (named: MATLAB_FRET_KT). In brief the following steps were performed: manually define ROI (masking nearby cells/aggregates), mean background calculation per channel, mean kinetochore/centromere calculation per channel and saving values to spreadsheet. FRET ratios were calculated using custom written MATLAB code ([67], kindly provided by M. Lampson, University of Pennsylvania), where adjustments to the script were made to readout spreadsheet containing parameters calculated in Fiji and generate donor/acceptor FRET images. An additional MATLAB script was written (kindly provided by S. Sonneveld) to batch-process all images for a single condition and assemble the FRET ratios in a single spreadsheet files for either local or object ratios computed.

Quantification of aligned versus unaligned in the CENP-E-inhibited conditions was done on the max. projected image of local FRET ratios. A manual ROI was defined to select the aligned objects followed by thresholding (Otsu) to create an ROI for measurement of the FRET ratio of all aligned objects. Similarly, unaligned objects were measured by inverting the ROI (excluding aligned objects). Live cell kinetochore intensities of mCherry-BUB1 were quantified by using the FRET channel as kinetochore position reference and mCherry background was subtracted (see MATLAB_FRET_KT code). Data was normalized over mean mCherry-BUB1 intensity in nocodazole condition.

Organoid data was processed using Imaris XT 9.3.1 (bitplane.com) and the plugin XT Mean Intensity Ratio (open.bitplane.com). The XT Mean Intensity Ratio code was rewritten to run on MATLAB Runtime Compiler 8.0 (kindly provided by S. Sonneveld). Image data was duplicated and a background subtraction and Gaussian filter were applied. When possible, surface tracking of H2B nuclei was performed semi-automated, in other instances manual ROI were defined using adaptive thresholding. The mTurquoise2 and FRET quantifications were performed on raw imaging data. Mean donor/acceptor ratio per nucleus was computed using XT mean ration intensity and data was exported and normalized to first frame (±45 min before NEB). All FRET data was computed on an HP-Z440 workstation (Xeon 3Ghz E5-1660 v3, 96GB RAM, AMD FirePro W7100).

All statistical analysis was performed using Prism (8.2.1, GraphPad) where normality test was performed (D'Agostino & Pearson) and subsequently One-way Analysis of Variance (ANOVA) with Tukey's multiple comparison test were performed to compare experimental groups when $n \geq 3$ independent replicates were quantified. Analysis of data presented in Figures 1D and 3C, 3D, and 3F was performed by fitting sigmoidal curves with least square nonlinear regression ($R^2 \geq 0.94$) to test statistical significance of reduced/increased MPS1sen activity signaling. To quantify the speed of MPS1 activation the first derivative was calculated followed by linear regression on the linear part of the activation slope ($R^2 \geq 0.97$). To quantify premature activation of MPS1sen, two-way ANOVA was performed on the mean at each time point followed by Tukey's multiple comparison test and significance score was adjusted by taking multiple comparison into account. The standard deviation, standard error of the mean or 95% confidence interval of the mean were computed using Prism.